Pt-WO3 oxydehydrates fructose to furans in the gas phase

(Article begins on next page)

31 December 2024

Pt-WO$_3$ oxydehydrates fructose to furans in the gas phase

Davide Carnevali[a], Adrien D'Oliveira[a], Marco G. Rigamonti[a], Fabrizio Cavani[b], Gregory S. Patience[a]

[a]*Polytechnique Montréal, Chemical Engineering, CP 6079, Succ CV, Montreal, PQ H3C 3A7, Canada*
[b]*University of Bologna, Chimica Industriale, Viale del Risorgimento, 4, 40136 Bologna, Italy*

Abstract

Bio feedstocks are destined to replace fossil fuels for specialty chemicals but current biorefineries mainly ferment hexose—the most abundant feedstock—to ethanol. The maximum theoretical carbon atom efficiency of this process is 67 % but the market price of biofuels is several-fold lower than biochemicals and monomers. We report for the first time a gas phase catalytic process that dehydrates fructose to 5-hydroxymethyl furfural (HMF). A two-fluid nozzle atomizes aqueous solutions of fructose into a fluidized bed operating at 350 °C. The solution forms an aerosol (droplet size of 30 µm), which contacts the hot Pt-WO$_3$/TiO$_2$ catalyst and reacts to HMF rather than caramelizing. The maximum yield reached 21 % and it increased slightly with temperature, and decreased with increasing catalyst inventory; it was less sensitive to O$_2$ concentration, Pt loading on the catalyst, liquid feed flow rate, and fructose feed concentration. At the optimal condition, selectivity continued to increase with time even after 3 h reaction. Selectivity to 2,5-diformyl furan reached 42 % at 250 °C with HMF as a feedstock.

Keywords: fluidized bed, oxydehydration, frucotse, platinum, atomization, 5-hydroxymethyl furfural

1. Introduction

The elevated oxygen/carbon ratio of carbohydrates versus petroleum constitutes an advantage to produce specialty chemicals and monomers. Sugar fermentation to bio-ethanol dominates the market at a maximum theoretical carbon atom yield of 67 % [1]. However, specialty chemicals command prices several-fold higher than that of bioethanol at fuel value. Fructose dehydrates to 5-hydroxymethyl furfural (HMF), a green intermediate, with a greater selectivity than glucose due to the similar spatial conformation and the faster enolisation reaction [2]. Hydrogen reacts with HMF to dimethyl furan and dimethyl tetrahydrofuran (Figure 1)—a biofuel [3, 4]— while the hydrogenolytic ring opening produces adipic acid—a monomer for nylon-6,6 [5]. Oxygen reacts with HMF to 2,5-diformyl furan [6, 7, 8] and further to 2,5-furandicarboxlylic acid (FDCA) [9, 10] . FDCA is the furanic substitute of terephthalic acid, which is a promising substitute for polyethylene terephthalate. Avantium developed the YXY technology that converts HMF to an ether with methanol/ethanol followed by an oxidation step to FDCA [11, 12]. Acidic catalysts, ionic liquids, and supercritical water dehydrate fructose and glucose to HMF [13, 14, 15, 16, 17, 18, 19]. Organic solvents are necessary to extract the product otherwise HMF hydrolyzes to levulinic acid and formic acid, or polymerizes to insoluble compounds—humins [20, 21, 22] (Figure 1).

Sn-Beta zeolite in tetrahydrofuran and water convert carbohydrates at 70 % selectivity [23]. Other organic solvents include alkylphenol [24], dimethylsulfoxide (DMSO) and methylisobutylketone [25, 26] and ethyl acetate [27]. These processes require contact times that range from minutes to hours because of the poor mass and heat transfer characteristics of multiphase (liquid) reactors.

Metal-based catalysts [9, 10, 28, 29, 30, 31] or enzymatic processes [32, 33, 34] oxidize HMF to FDCA. Tandem processes in a single vessel reduces complexity

²⁸ like the multiphase reactor with methyl-isobutyl ketone and 2-butanol as organic

²⁹ phase [35]; the aqueous solution dehydrates fructose to HMF, while the organic

³⁰ phase extracts it and further oxidizes to FDCA [36]. Pt/C oxydehydrates fruc-

³¹ tose to FDCA in γ-valero lactone and H_2O [37]. Combination of ionic liquids

³² and not-noble metals avoid the organic phase and allows the one pot reaction

³³ [38]. Fluidized bed reactors operate at higher temperature with superior mass

³⁴ transfer and, consequently, reaction rates orders of magnitude higher. FBRs

³⁵ pyrolyze biomass into energy and chemicals [39]. Glass beads in an FBR cracks

³⁶ aqueous solutions of sugar sparged into the bed [40, 41] Fast pyrolysis of cellulose

³⁷ in FBRs approach 62 % yields of levoglucosan, 3.5 % of HMF and 1 % of furfural

³⁸ [42]. Immobilized anaerobic sludge produces biohydrogen and bioethanol [43].

³⁹ A magnetically stirred fluidized bed reactor ferments glucose to ethanol within

⁴⁰ 95 % of the theoretical yield [44]. Two anaerobic fluidized bed reactors at 55 °C

⁴¹ product H_2 and ethanol molar fractions of 59 % for a xylose-glucose mixture

⁴² [45].

⁴³ We demonstrated the versatility of atomizing liquids into catalytic fluidized

⁴⁴ beds: VPO partially oxidizes xylose to C2-C4 carboxylic acids [46]; WO_3/TiO_2

⁴⁵ dehydrates glycerol to acrolein [47]; decarbonylates fructose to furfural [48]; and,

⁴⁶ Keggin-type catalyst oxydehydrates 2-methyl,1-3-propanediol to methacrylic

⁴⁷ acid [49]. Here we investigated fructose dehydration to HMF in a μ-fluidized

⁴⁸ bed reactor. A nozzle atomized the aqueous liquid feed directly into the cat-

⁴⁹ alytic bed. We screened temperature, O_2 concentration, catalyst loading, Pt

⁵⁰ content on the catalyst, liquid flow rate, feed fructose mass concentration with

⁵¹ a Plackett-Burman experimental design. The experimental plan was based on

⁵² three levels of temperature and O_2:fructose molar ratio and two levels for cata-
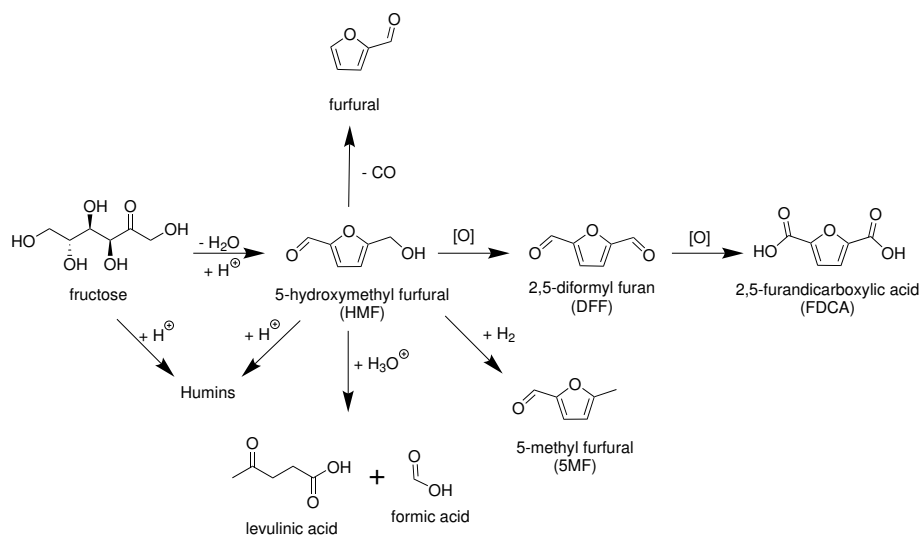
⁵³ lyst loading.

Figure 1: Fructose dehydrates to HMF. Organic solvents suppress the polymerization to humins and the rehydration to levulinic acid and formic acid. Decarbonylation leads to furfural, while the hydrogenation produces 5MF. HMF oxidation gives DFF and further FDCA, the furanic substitute of terephthalic acid.

2. Experimental section

A furnace heated a 15 mm ID by 400 mm high quartz tube. Three thermocouples measured the temperature along the length at 20 mm below the bed, 5 mm — inside the bed, 90 mm above the distributor, and a fourth monitored the temperature in the exit line. The reactor operated at 1.4 bar while the ΔP between the inlet and outlet—0.001 bar during the reaction. A quartz frit, with a porosity of 150 µm to 200 µm, ensured the gas was distributed uniformly across the reactor diameter (Figure 2). A stream of O_2 in Ar fluidized the catalytic bed and burned the coke formed during the reaction. A nozzle atomized the aqueous fructose solution into the Pt-WO$_3$/TiO$_2$ catalytic bed. An HPLC pump metered the liquid solution feedrate while $50 \, \mathrm{mL \, min^{-1}}$ of argon atomized it to produce an effervescent spray (Figure 3c) with droplets less than 30 µm to minimize catalyst agglomeration and blocking the nozzle. A ceramic tube enveloped the injector to reduce the heat transfer and ensure that the solvent
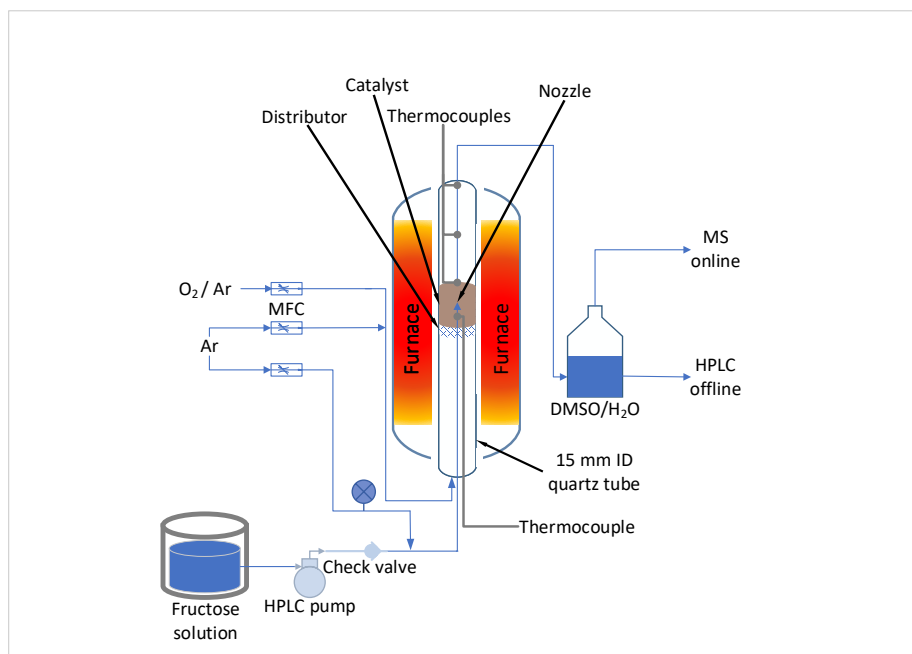
4

Figure 2: A nozzle atomizes the fructose solution directly into the catalytic bed. A DMSO/H$_2$O quench traps the products and an HPLC analyzes the trend. An online MS monitored non-condensable gases.

evaporated in the bed rather than the injector; A stream of $50\,\mathrm{mL\,min^{-1}}$ of argon flushed the annular space between the injector and ceramic tube. The exit line (uninsulated) fed into a quench in an ice bath The quench fluid contained $25\,\mathrm{g}$ dimethyl sulfoxide to improve furanic solubility and $25\,\mathrm{g}$ H$_2$O. An on-line mass spectrometer (MS) with a multiple ion detector monitored non-condensable gas concentrations—CO, CO$_2$, O$_2$, Ar, CH$_4$, while an HPLC quantified the liquid samples collected each $15\,\mathrm{min}$ during the first hour and then each $30\,\mathrm{min}$ until the end of the experiment (Figure 2). Glycerol was the internal standard for the HPLC analysis. At the end of each experiment we cleaned the exit line with $5\,\mathrm{mL}$ of water and analyzed this sample.

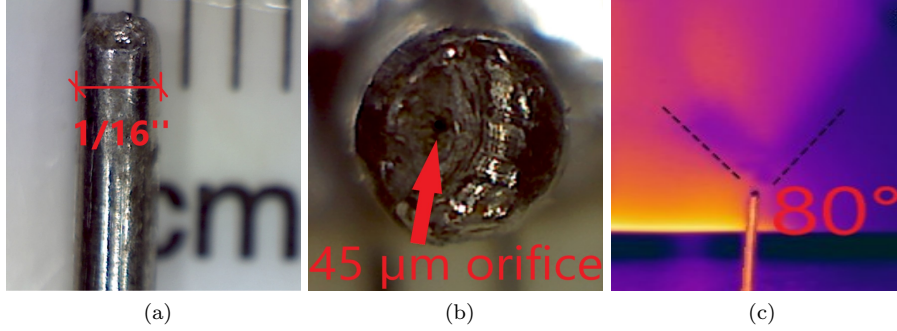Product selectivity, S_i, is based on a molar balance around each component i, n_i^{out}:

Figure 3: 1/16" (1.59 mm) stainless steel pipe filed at the top to obtain an orifice of 45 µm. The IR camera shows that the atomization and the evaporation at the orifice decreased the temperature at the tip, forming a full cone with an angle of 80°.

$$S_i = \frac{\Sigma_j n_{i,j}^{\mathrm{out}}/\vartheta_{i,j}}{n_{\mathrm{fr}}^{\mathrm{in}} - n_{\mathrm{fr}}^{\mathrm{out}}} \cdot 100 \tag{1}$$

where $n_{\mathrm{fr}}^{\mathrm{in}}$ and $n_{\mathrm{fr}}^{\mathrm{out}}$ are the moles of fructose entering and exiting the system and ϑ_i is the stoichiometric coefficient for the carbon component of each reaction j. The median droplet size diameter, d_{50}, exiting the nozzle of an internal mixing air-assist atomizer is [50]:

$$d_{50} = 20 \ u_{\mathrm{L}}^{0.5} \ m_L^{0.1} \ d_L^{0.1} \ \sigma^{0.2} \ \rho_g^{-0.3} \ \Delta U^{-1.0} \ \left[1 + \frac{m_{\mathrm{L}}}{m_{\mathrm{g}}}\right]^{0.5} \tag{2}$$

where u_{L} is the superficial velocity, m_{L} and m_{g} the mass flow of the liquid and the gas, d_{L} the orifice dimension, σ is the surface tension and the ΔU the relative velocity between the liquid and the gas.

2.1. Materials

All the reagents are analytical grade without further purification. We acquired D-fructose(99 %) from Alfa Aesar. We purchased 5-hydroxymethyl furfural (99 %), furfural (99 %), 5-hydroxymethyl-2-furancarboxylic acid, 5-formyl-2-furoic acid, 2,5-furandicarboxylic acid (97 %), 2,5-furandicarboxaldehyde (97 %),

92 5-methyl-2-furaldehyde ($\geq 98\%$), and tetraammineplatinum(II) nitrate ($\geq 99.9\%$)

93 and ammonium (para)tungstate hydrate ($>99.99\%$) from Sigma Aldrich. Air

94 Liquide Canada supplied the gases: argon ($> 99.7\%$), 10.0% O_2 balance Ar, and

95 a mixture of CO (1.04%), CO_2 (1.01%), CH_4 (1.03%) balance Ar. Huntsman

96 Corporation supplied the titanium dioxide (Hombikat 110100).

2.2. Catalyst preparation

98 We sieved the support powder from $90\,\mu m$ to $150\,\mu m$ in diameter. The crys-

99 talline phase of the titania was pure anatase. A successive wetness impregnation

100 method deposited first WO_3 and then Pt on the TiO_2 support. Initially we de-

101 termined the total pore volume by dropwise addition of water. Ammonium

102 paratungstate dissolved in a volume of water equivalent to the pore volume of

103 the support. A rotary evaporator operating at 100 rpm for 3 h mixed the active

104 phase and support. The catalyst then dried at $70\,°C$ and $300\,mbar$ for 2 h. The

105 powder then calcined in a furnace at $120\,°C$ for 4 h to completely remove traces

106 of water. The furnace then ramped temperature at $2.5\,°C\,min^{-1}$ to $600\,°C$ in

107 air. The powder remained in the furnace at this temperature for 4 h.

2.3. Analytical instrumentation

109 A Philips X'PERT diffractometer generated XRD spectra with a monochro-

110 matic Cu-kα beam, $\lambda = 0.154\,06\,nm$, at $50\,kV$ and $40\,mA$. It scanned the

111 gonio axis from $20°$ to $85°$, at a rate of $0.01\,°\,s^{-1}$. The crystalline phases were

112 identified with the ICDD database and the Rietveld refinement (X'PERT high-

113 score) gave a semi-quantitative characterization for the phases' weight compo-

114 sition. The Scherrer approximation defined the average cubic crystallite size:

115 $D = 0.94\lambda/\beta Cos\theta$, where λ is the mentioned instrument wavelength, β is the

116 full-width at half-maximum peak height (FWHM, rad), and θ is the Bragg angle

117 for the most intense peak (half of the 2θ position).

The FE-SEM-JEOL JSM-7600F scanning electron microscope (SEM) acquired the catalyst images between 5 kV to 30 kV, using secondary and backscattered electrons detectors (secondary electron image —SEI, low secondary electron image —LEI and backscatter image —LABe). The energy dispersive X-ray detector (EDX) mapped the surface of the catalyst and qualitatively quantified the composition and the different phase regions.

A laser diffractometer (Horiba, LA-950) evaluated the particle size distribution (PSD) based on the Mie Theory:

$$D_{4,3} = \frac{\sum d_i^4 \cdot N_i}{\sum d_i^3 \cdot N_i} \tag{3}$$

with N_i as number of particles with diameter d_i. The particle refractive index was $2.75 + 0.00i$ (R and Chi parameter below 0.05).

A Quantachrome Autosorb-1 N_2 physisorption instrument recorded the adsorption and desorption isotherms at 77 K. A degasser, operating under vacuum at 300 °C for 6 h, removed the gas adsorbed on the surface [51]. The Brunauer-Emmett-Teller (BET) theory regress the specific surface area at P/P_0 0.05 to 0.3. The instrument estimated the mesopore size distribution over the desorption branch (P/P_0 0.15-0.995), based on the Barrett-Joyner-Hallender (BJH) theory. The total pore volume is evaluated at the maximum filling pressure (P/P_0 0.995), considering all pores with a diameter smaller than 300 nm.

A LECO CS744 CHN analyzer measured carbon build up on the catalyst surface after each experiment. An internal balance measured the sample weight loss, when heated above 1000 °C in air. A further CO trap converted the remaining carbon monoxide to CO_2.

A Varian ProStar 325 HPLC, equipped with a UV detector at 260 nm, quantified species concentration of the liquid samples. A MetaCarb 87H column, kept at 60 °C, separated the compounds. The pump flowed a 0.05 N aqueous H_2SO_4

^{143} solution at $0.35\,\mathrm{mL\,min^{-1}}$. Each analysis lasted $70\,\mathrm{min}$ to ensure the products

^{144} separation.

^{145} **3. Results and discussion**

^{146} *3.1. Catalyst characterization*

^{147} *3.1.1. Fluidization and particle size distribution*

^{148} Geldart classified particles into 4 categories based on the catalyst diameter

^{149} and the differential of the particle density and the gas density [52]. Geldart

^{150} group A powders are best suited for catalytic fluidized beds with diameters

^{151} (d_{50}) on the order of $70\,\mathrm{\mu m}$. Based on the Horiba LA-950, the average spher-

^{152} ical particle diameter of fresh catalyst increased from $85\,\mathrm{\mu m}$ to $95\,\mathrm{\mu m}$ (Figure

^{153} 4). Coke covered the surface (SEM-EDX) and increased the average particle

^{154} diameter by $10\,\mathrm{\mu m}$. The bulk density was $770\,\mathrm{kg\,m^{-3}}$, so that we classify it as

^{155} a group A powder.

^{156} The minimum fluidization velocity, u_{mf}, with $3\,\mathrm{g}$ of catalyst in the reactor

^{157} was $8\,\mathrm{mm\,s^{-1}}$. Catalyst attrition resistance is a major concern for fluidized

^{158} beds particularly with high velocity jets where particles collide and fragments or

^{159} cleaves surface asperities. To prevent this phenomena we opted for the catalyst

^{160} synthesis by incipient wetness impregnation, which minimizes surface defects

^{161} and thus asperities. We tested the attrition rate in an air jet mill according to

^{162} the ASTM 5757 [53]. The high velocity simulates the mechanical stress coming

^{163} from the nozzle and the distributor. A filtered vessel collected the elutriated fines

^{164} after $24\,\mathrm{h}$. The catalyst attrits at $5.4\,\mathrm{mg\,h^{-1}}$, which is well within commercial

^{165} practice [54].

^{166} *3.1.2. XRD*

^{167} We analyzed the calcined catalyst before reaction with a mass fraction of $5\,\%$

^{168} WO_3 on TiO_2 and $0.5\,\%$ Pt or $1.5\,\%$ Pt. We characterized the catalyst at the end
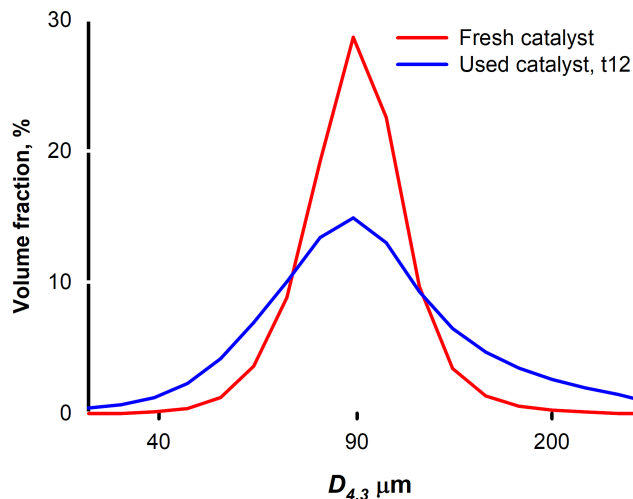
9

Figure 4: Catalyst particle size distribution in logarithmic scale. Coke deposits broadened the peak and increased the average.

Table 1: Variation of the catalyst physical characteristics after the reaction

Property	Fresh	Used
d_{50}, µm	85	95
SA, $\mathrm{m\,g^{-2}}$	51.4(1)	71(2)
V_{pore}, $\mathrm{mL\,g^{-1}}$	0.165	0.064
u_{mf}, $\mathrm{mm\,s^{-1}}$	8	
ρ_{bulk}, $\mathrm{kg\,m^{-3}}$	770	
Attrition resistance, $\mathrm{mg\,h^{-1}}$	5.4	5.4

of experiment t12 (1.5 % Pt), which had the most coke. XRD analysis detected two crystalline phases: anatase for the titania (ref: 96-900-9087) and platinum (ref: 96-101-1114) while EDX confirmed the presence of W since it was below the XRD detection limit [48]. The titania support maintained a tetragonal structure during calcination and reaction. The platinum presented a cubic structure, with a submicron crystallinity, which increased with Pt loading and decreased due to the coke deposition during the reaction. SEM confirmed the results, providing images of crystals with several hundred nanometers size and a round-prismatic shape. Each crystal contained several crystallites, growing in different directions

Table 2: D crystallite size (standard deviation among Pt signals); Riet.Pt Rietveld refinement of the Pt phase, the complementary fraction was anatase TiO_2; BET surface area by nitrogen physisorption, results are within $\pm 3\,\%$ ($n = 3$, $95\,\%$ confidence interval, CI); ϕ pore volume (CI $\pm 8 \times 10^{-5}\,\mathrm{mL\,g^{-1}}$); $\Delta_{\mathrm{d}S(d)}\mathrm{d}S(d)$ characteristic pore median (ads. BJH for mesopore and QSDFT for micro); $V - t$ micropore area.

WO_3/TiO_2	D nm	Riet. Pt $\mathrm{g\,g^{-1}}$	BET $\mathrm{m^2\,g^{-1}}$	V_{pore} $\mathrm{mL\,g^{-1}}$	$\Delta_{\mathrm{d}V(d)}$ nm	$V - t$ $\mathrm{m^2\,g^{-1}}$
	na	na	63.8(0.1)	0.180	9.6(0.1)	4.3(0.5)
0.5 % Pt	52(7)	0.008	na	na	na	na
1.5 % Pt	88(2)	0.03	51.4(0.1)	0.165	11.0(0.1)	1.0(0.5)
Used, t12, 1.5 % Pt	60(10)	0.02	71(2)	0.064	0.7(0.3)	50(2)

178 (Figure 9). At $50\,\mathrm{kV}$, the X-ray penetrated the catalyst down to $35\,\mathrm{\mu m}$ (Pott's

179 equation): this surface analysis overestimated the Pt fraction with respect the

180 TiO_2 support. As coke builds up, the intensity of the Pt signals decrease and

181 broaden (Table 2). During calcination, WO_3 precursor penetrated the titania

182 lattice thereby reducing the tungsten signal. Calcination at $600\,^{\circ}\mathrm{C}$ was low

183 enough to minimize phase segregation and so the WO_3 remained amorphous.

184 A weak, unidentified peak emerged at 31.6° after reaction. Reaction conditions

185 may have crystallized part of the amorphous WO_3 in the mesoporous titania

186 structure however, SEM-EDX could not confirm WO_3 crystals on the surface of

187 the catalyst but N_2 physisorption detected a decrease in pore size after reaction.

188 The small crystallite size ($30\,\mathrm{nm}$) and the strong chemical interaction with the

189 surrounding environment (coke and titania) shift the signal.

190 *3.1.3. BET*

191 The TiO_2 support and tungsten salt precursor contribute most to the specific

192 surface area (SSA), pore size distribution and pore volume (PV) of the catalyst

193 after calcination (Figure 6) [48]. Calcined catalyst has a type IV isotherm and

194 an $H2$ hysteresis loop: mesoporous structurewith a narrow distribution of pore

195 necks. A mass fraction of $1.5\,\%$ Pt decreased the SSA with respect to calcined

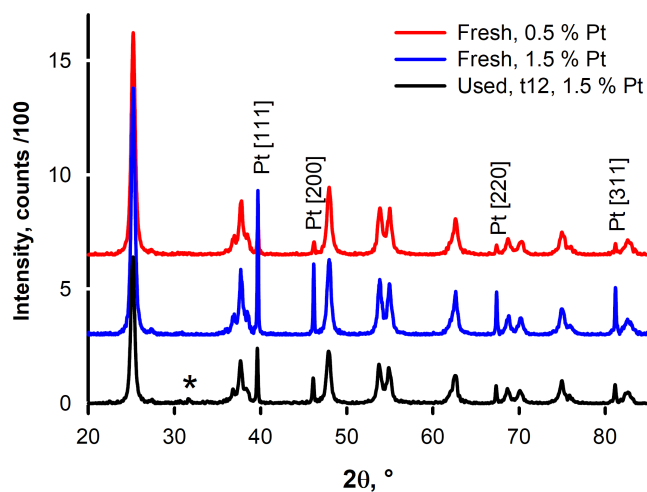196 WO_3/TiO_2 catalyst. EDX images show Pt on the surface but not in the interior

Figure 5: Stacked spectra recorded with the same conditions and smoothed with an 11 points cubic function, Cu-$k\alpha$ sidebands were removed: coke deposits on the used sample reduced the signal to noise ratio. Four sharp Pt signals (39.6°, 46.0°, 67.4°, 81.2°) and their respective planes [hkl] have been identified. The remaining peaks belong to the titania support (anatase) [55].

so the drop in SSA and PV is due to pore-blocking. Pt obstructed pores smaller than 10 nm, which increased the characteristic pore median ($\mathrm{d}S(d)$) by 1 nm. The "t12" catalyst has a type I-IV isotherm and an open $H4$ hysteresis: a microporous network developed as coke partially filled the internal mesoporous structure. Despite coke deposits, furanic selectivity improved with time. The SSA increased with respect to calcined catalyst, suggesting a selective coke deposit. This phenomenon decreased the reagent and product degradation, despite the pore size dropping from 11.0 nm to 0.7 nm) and the lower pore volume (Table 2). The BJH surface distribution shrunk in the mesopore region. The quenched solid state functional theory (QSDFT) for SSA deviated less than 5 % from the BET SSA.

3.1.4. Field Emission Scanning Electron Microscopy (FE-SEM)/EDX

The tungsten oxide was homogeneously dispersed on the titania support. Pt crystals were poorly dispersed on the surface as SEM images show regions
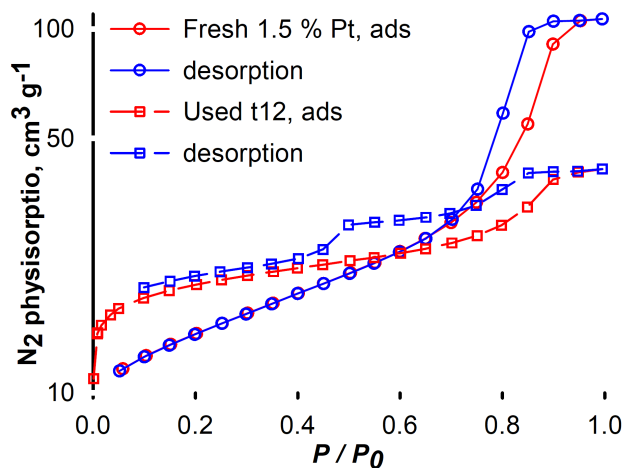
12

Figure 6: Nitrogen physisorption isotherms. The used catalyst loses the microporous fraction and the total pore volume decreases as a consequence. Carbon obstructing the mouth of the micropores accounts for the large reduction at $P/P_o > 0.7$.

with bright spots with Pt particles (Figure 7). Furthermore, some particles have much more Pt than others. The Pt submicron crystals were $250\,\mu m$ on average (Figure 8). After reaction, Pt particles formed agglomerate with several hundred crystals but the powder remained free flowing. Only on the sparger tip circumference did powder agglomerate [46].

An EDX scan at $20\,kV$ of the catalyst surface to a depth of $10\,\mu m$ confirmed that W covered the surface uniformly. On the contrary, Pt forms submicron crystals rather than forming a monolayer on the surface or in the interior. Titanium-oxygen molar ratios were coherent with the TiO_2 composition. Pt was only in the metallic form since the EDX oxygen image showed dark spots corresponding to the Pt crystals (Figure 10).

We crushed used catalyst and the SEM images of the chunks showed no coke in the interior. As much as $(20\,\mu m)$ of coke covered some of the particles but most of it was homogeneously distributed on the surface (Figure 10). Clearly, since the carbon coverage was uniform WO_3 rather than Pt initiated the growth of the coke layer. An EDX spectrum on the coke deposit identified a molar
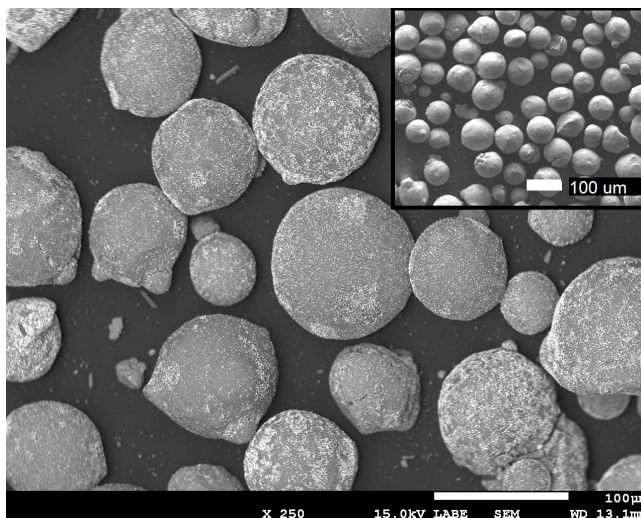
Figure 7: Fresh 1.5 % Pt over WO$_3$/TiO$_2$ particles. The LABe detector enhanced the signal from heavy elements and the Pt crystals appeared as bright white spots.

composition of 90 % soft carbon type and 10 % oxygen.

3.2. Internal-mixing two-fluid nozzle

Operating the fluidized bed was problematic due to frequent interruptions in the fluid flow due to solids build up in the sparger. The large surface to volume ratio of the sparger was a contributing factor as the water would evaporate in the tube and the fructose would then crystalize. We injected Ar at $50\,\mathrm{mL\,min^{-1}}$ to reduce the residence time of the solution in the tube and improve the effervescent spray of the liquid. The gas and fluid first mix at the t-junction below the sparger tip. We reduce the internal diameter of the top part of a stainless steel pipe of 1.6 mm OD and 0.127 mm ID (Figure 3a) to create a 45 µm±5 µm orifice (Figure 3b), which is a 65 % reduction of the internal diameter. The setup produced a full cone spray with an angle of 80°±5°, measured by infrared camera after heating the nozzle to 400 °C.

Based on Equation 2, the median droplet size was 5 µm, with a Weber number of 7. The gas flow was laminar around the particles ($N_{\mathrm{Re}} = 11$) and at the
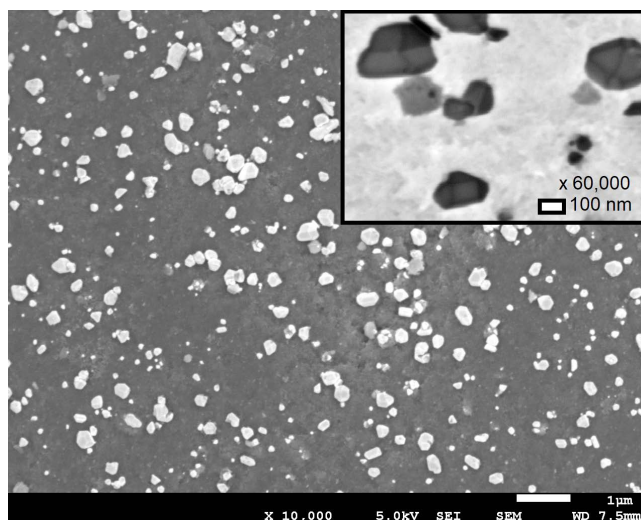
14

Figure 8: Fresh 1.5 % Pt over WO$_3$/TiO$_2$ particles. The metallic platinum crystals appeared as multi-facets prisms. Considering their sizes (submicron), the crystallite size of 88 nm (XRD) and the crystal structure of metallic Pt (cubic), several crystallites compose the crystal.

orifice ($N_{\mathrm{Re}} = 750$). Higher Re and We numbers increase the atomization speed and reduce the droplet diameter. Internal mixing increased the contact between the gas and the liquid producing finer droplets [50].

3.3. Screening test and full factorial design

A Plackett-Burman screening design assessed the influence of six factors: temperature (150 °C and 300 °C), O$_2$:fructose molar ratio (2:1 and 20:1), catalyst mass (2.5 g and 5 g), Pt loading (0.5 % and 1.5 %), feed flow rate (50 µL min^{-1} and 100 µL min^{-1}) and feed fructose mass concentration (2.5 % and 5 %). The design comprised 12 experiments.

All the tests demonstrated total conversion of fructose and produced coke, COx, and various organic compounds. Some of the fructose degraded along the walls and exit line.

The dehydration reaction was independent of oxygen concentration but it helped control coke build-up on the surface. The two levels of mass of catalyst
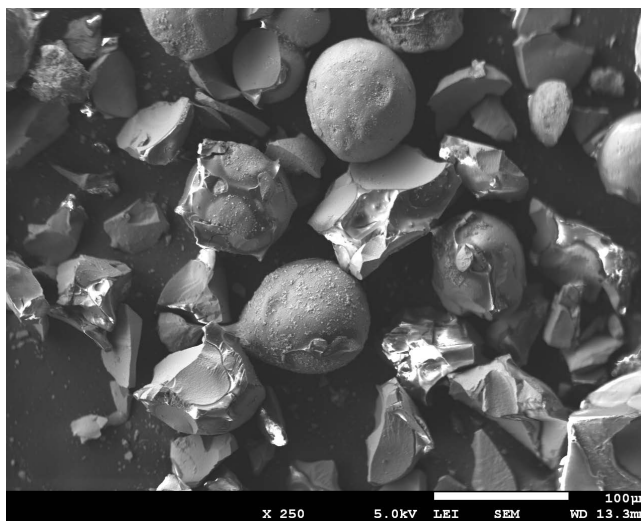
15

Figure 9: Used "t12" catalyst's surface. Shiny "metallic-lookalike" coke chunks were dispersed around the spherical catalyst particles after mechanical breakage. Some particles broke as well.

loaded varied the contact time, while two flow rates modified the weight hour space velocity and the gaseous partial pressure of water.

Catalyst loading accounted for most of the variance in the data: furanic products selectivity was greater with less catalyst. The maximum total product selectivity never exceeded 6%, due to the extreme conditions of the screening test. CO_2 and CO rose with temperature, reaching 59% and 4% at $300\,°C$, respectively. Furthermore, higher oxygen concentration produced more CO_2. HMF, the dehydration product, increased with higher liquid flow rate and lower catalyst loading. Increasing the partial pressure of water increased the catalytic surface saturation, lowering the degradation kinetics. HMF conversion increased with higher contact time. Furfural, the decarbonylation product of HMF (Figure 1), depended only on catalyst loading—it increased with longer contact time. Maximizing the contact time, determined the fructose and the intermediate degradation to coke and COx. HMF hydrodehydrates to 5MF (Figure 1). Higher temperature and lower catalyst loading increase selectivity.
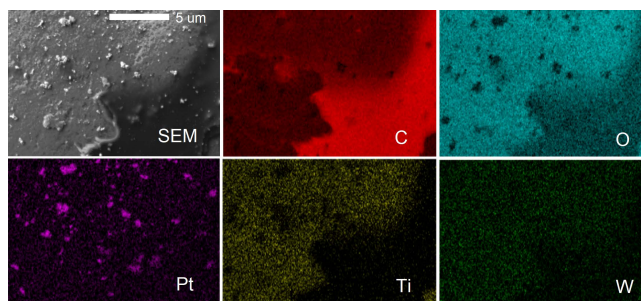
16

Figure 10: SEM and EDS mapping of the used "t12" catalyst's surface. Carbon (C, red) partially covered the surface and suppressed the underlying elements' signals. Oxygen (O, blue) was predominant were titanium was also present (Ti, yellow), less were carbon was present and absent were platinum was present (Pt, violet). Tungsten (W, green) was homogeneously distributed along with titanium.

Furthermore, lower O_2 concentration reduces the conversion of H_2 to water, increasing the hydrogenation reaction rate. Increasing the Pt favoured hydrogen adsorption, and consequently 5MF.

Oxygen reacts with HMF to HMFCA and DFF (Figure 1). Oxidation kinetics of the hydroxyl moiety of HMF is faster than the conversion of the aldehydic functional group. DFF only reached a maximum selectivity of 1%, while HMFCA never exceeded 0.05%. Lower catalyst loading and higher temperature increased the selectivity, which is consistent for a high activation energy for HMF oxidation. Furthermore, as for all the furanic compounds, lower catalyst loading reduced the contact time and the degradation process. A further oxidation of HMFCA and DFF led to FDCA. The amount of catalyst tested was high, leading to elevated contact time and increasing the degradation.

We executed a full factorial design including three levels for temperature (300 °C, 350 °C, and 400 °C) and O_2 content (0.5, 1 and 10 molar ratio with fructose) and two levels of catalyst loading (1.5 g and 3 g). We kept Pt loading (1.5 %) constant, increasing the liquid flow rate (300 μL min^{-1}) and keeping the fructose mass percentage in the feed at 2% (Table 3).

The contact time, τ, between the fructose injected and the catalyst varied

Table 3: Fructose oxydehydration full factorial design of experiments over 1.5 % Pt-WO_3/TiO_2. Factors include catalyst loading (2 levels), temperature (3 levels), and O_2:fructose molar ratio 3 levels). The selectivities are calculated from time 0 min to 180 min. HMF: 5-hydroxymethyl furfural; FUR: furfural; 5MF: 5-methyl furfural; DFF: diformyl furan.

Exp #	Cat g	T °C	O_2/fruct	S_{CO_2} %	S_{CO} %	S_{CH_4} %	S_{Coke} %	S_{HMF} %	S_{FUR} %	S_{5MF} %	S_{DFF} %
1	3	300	0.5	6	6	9	8	0	5	3	1
2	3	400	1	12	10	5	10	4	5	1	1
3	1.5	300	10	20	4	17	6	6	4	0	1
4	1.5	400	1	2	3	1	12	9	3	0	0
5	3	350	10	4	3	4	55	3	2	1	1
6	3	300	1	3	12	2	43	3	1	0	0
7	1.5	350	10	0	2	0	21	1	1	0	0
8	3	350	0.5	8	5	4	54	0	5	4	3
9	1.5	300	0.5	2	0	1	13	0	1	0	0
10	1.5	300	1	4	2	3	36	5	6	1	1
11	3	350	1	12	6	5	57	1	5	4	3
12	1.5	350	1	7	5	5	49	11	6	1	2
13	1.5	350	0.5	4	3	4	31	12	6	1	1
14	1.5	400	1	7	3	5	48	7	3	1	3
15	3	400	10	47	1	17	43	0	0	0	0
16	3	300	10	41	1	15	66	1	2	0	1
17	3	400	0.5	4	2	2	24	1	9	6	2
18	1.5	400	10	11	8	3	20	0	7	4	2

between 0.3 s to 0.4 s and fructose conversion was complete for all experiments (Table 3). The carbon balance was between 57 % to 97 %. Carbon losses were due to product degradation on the reactor wall or inside the exit line. The catalyst becomes increasingly selective with time and this induction time can exceed 2 h so the reported selectivities are pessimistic since they are calculated based on the 3 h from when the pump started. The mass balance of several tests were less than 50 % so we have ignored these tests while assessing the impacts of the various factors. The sum of the selective oxidation products—HMF, furfural, 5-methyly furfural, and DFF—reached 20 %. The highest yield of DFF was only 3 % but HMF, the first step of the process, reached 12 %. According to a power-law regression model, the furanic's concentration increases linearly with temperature but decreases with the square root of mass of catalyst and decreases to a lower power with the oxygen:fructose ratio—feeding more oxygen reduces the productivity (Figure 11). The correlation explains 63 % of the variance in
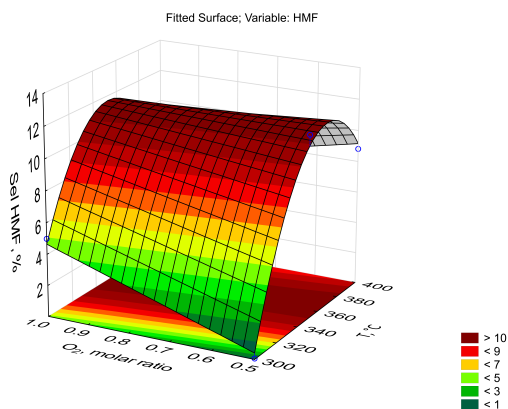
Figure 11: Surface chart of HMF selectivity with 1.5 g catalyst loading.

the data but excludes experiments for which the mass balance closure is less than 50 %. The reason relates to the temperature, which was too low to react.

The CO_2 selectivity reached 20 % while the maximum CO selectivity and CH_4 selectivity were 12 % and 17 %, respectively. The concentration of CO_2 was highly correlated with CH_4. Excluding experimental data for which the mass balance closed to below 50 %

$$CH_4 = 1.2 \frac{CO_2}{W} \quad R^2 > 0.9 \tag{4}$$

where W is the mass of catalyst (Figure 12). Data CO_2 selectivity was essentially independent of temperature; it increased with the square-root of the O2:fructose ratio, and increased more than linearly with the mass of catalyst. Considering the complete decompostion to the stoichiometric lowest common denominator, we would expect a strong correlation between S_{CO_2} and S_{CH_4}
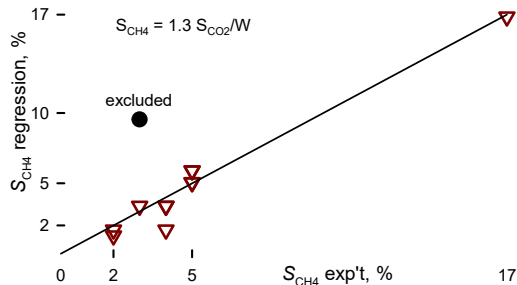
$$C_6H_{12}O_6 \rightarrow 3CH_4 + 3CO_2 \tag{5}$$

19
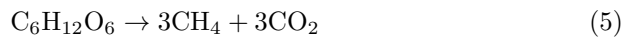
Figure 12: CH$_4$ parity plot. Data from 1 experiment was excluded because of the poor mass balance (closed circle).

or S_{CO} and S_{H_2O}

$$C_6H_{12}O_6 \rightarrow 6H_2O + 6CO \tag{6}$$

The strong correlation of the former could be related to the decomposition of a C$_2$ substrate like methylformate. Dimerization of formaldehyde leads to methylformate and this Tishchenko-like reaction is improbable at the reaction conditions. Feeding formalin across the reactor at these conditions would confirm this reaction mechanism. We exclude methanation as a reaction pathway and sequential combustion of methane from the oxygen in the fructose as this would produce water. Coke formation is related to the decomposition of the feed or the products on the catalyst and built up in all experiments and agglomerated.

3.4. HMF to DFF

We investigated the oxidation of HMF to DFF at four temperatures between 250 °C to 400 °C and two catalyst loading, 1.5 g and 5 g, maintaining the O$_2$:HMF molar ratio of 2 (Table 4). Higher catalyst loading reacted all the HMF at the expense of DFF selectivity which approached at most 4 %. On the other hand, at low catalyst loading and 350 °C or 400 °C DFF selectivity was 26 % and 16 %, respectively. Conversion dropped to 86 % at 250 °C and DFF selectivity increased to 42 %.

20

Table 4: Higher contact time increase the degradation kinetic. Decreasing the temperature decreases the conversion but raise the DFF selectivity. The O_2:HMF ratio was 2 for all experiments.

| Mass | T | Conversion | S_{CO_2} | S_{CO} | S_{FUR} | S_{5MF} | S_{DFF} |
g	°C	%	%	%	%	%	%
1.5	350	100	6	6	9	11	26
5	350	100	4	6	0	1	0
1.5	400	100	23	6	4	12	16
5	400	100	11	5	1	2	4
1.5	300	92	3	28	1	11	15
1.5	250	86	15	18	6	18	42

5MF, the main by-product of the reaction, is mainly controlled by temperature and catalyst inventory. In fact, at higher contact time, the selectivity dropped to 2 %, while decreasing the temperature from 400 °C to 200 °C, the selectivity increased from 12 % to a maximum of 18 %. Furfural, the other main by-product, remained almost stable around 6 % for all the reactions with lowest amount of catalyst, but ranged was 1 % with 5 g of catalyst Coke built up on the catalyst, but was insensitive to either temperature or catalyst loading.

CO and CO_2 the selectivity varied considerably with both temperature and catalyst loading. At low temperature and low catalyst loading, CO was higher than CO_2, but increasing the two variables, the ratio became 1:1 and with a further increase CO_2 selectivity became higher than that of CO. The higher contact time increased the degradation of the molecules and carbon oxide selectivity increased with temperature.

4. Conclusions

Gas phase fructose oxydehydration is a new pathway to platform chemicals from organic feedstocks. It avoids organic solvents, decreases reaction time to fractions of a second, and facilitate product separation. Fructose first dehydrates to HMF followed by tandem reactions to furfural, 5-MF, and DFF.

Other undesirable products are CO, CO_2, CH_4, and coke. The CH_4 is linearly correlated with CO_2 while the selectivity to coke was highest among the products detected. Generally, the mass balance was greater than 50 % but for 5 of the 18 experiments in the full factorial design it was less than this. HMF selectivity from fructose reached 12 % at 350 °C. Other partial oxidation product selectivities were less than 7 %. Even shorter contact times are required to improve selectivity and reduce conversion. Since the catalyst induction time was on the order of 2 h (the catalyst continued to activate), the product selectivities are certainly higher. Coke built up on the catalytic surface, agglomerated the catalyst but also covered the strongest acid sites, enhancing the selectivity to the furanic compounds. Feeding HMF rather than fructose demonstrated that lower temperatures are required to increase the furanic's selectivity.

Acknowledgments

References

[1] S. Macrelli, J. Mogensen, G. Zacchi, Techno economic evaluation of 2nd generation bioethanol production from sugar cane bagasse and leaves integrated with the sugar based ethanol process, Biotechnology for Biofuels 5 (2012) 22. doi:10.1186/1754-6834-5-22.

[2] A. A. Rosatella, S. P. Simeonov, R. F. M. Frade, C. A. M. Afonso, 5-Hydroxymethylfurfural (HMF) as a building block platform: Biological properties, synthesis and synthetic applications, Green Chemistry 13 (4)

373 (2011) 754. doi:10.1039/c0gc00401d.

374 URL http://xlink.rsc.org/?DOI=c0gc00401d

375 [3] E. Taarning, C. M. Osmundsen, X. Yang, B. Voss, S. I. Andersen, C. H.
376 Christensen, Zeolite-catalyzed biomass conversion to fuels and chemi-
377 cals, Energy and Environmental Science 4 (2011) 793–804. doi:DOI:
378 10.1039/C004518G.

379 [4] N. Ly, K. Al-Shamery, C. E. Chan-Thaw, L. Prati, P. Carniti, A. Ger-
380 vasini, Impact of Support Oxide Acidity in Pt-Catalyzed HMF Hydro-
381 genation in Alcoholic Medium, Catalysis Letters 147 (2) (2017) 345–359.
382 doi:10.1007/s10562-016-1945-9.

383 [5] J. Tuteja, H. Choudhary, S. Nishimura, K. Ebitani, Direct synthesis
384 of 1,6-hexanediol from HMF over a heterogeneous Pd/ZrP catalyst us-
385 ing formic acid as hydrogen source, ChemSusChem 7 (1) (2014) 96–100.
386 doi:10.1002/cssc.201300832.

387 [6] C. Lucarelli, S. Galli, A. Maspero, A. Cimino, C. Bandinelli, A. Lolli, J. Ve-
388 lasquez Ochoa, A. Vaccari, F. Cavani, S. Albonetti, Adsorbent-Adsorbate
389 Interactions in the Oxidation of HMF Catalyzed by Ni-Based MOFs: A
390 DRIFT and FT-IR Insight, Journal of Physical Chemistry C 120 (28)
391 (2016) 15310–15321. doi:10.1021/acs.jpcc.6b05428.

392 [7] F. L. Grasset, B. Katryniok, S. Paul, V. Nardello-Rataj, M. Pera-
393 Titus, J.-M. Clacens, F. De Campo, F. Dumeignil, Selective ox-
394 idation of 5-hydroxymethylfurfural to 2,5-diformylfuran over interca-
395 lated vanadium phosphate oxides, RSC Advances 3 (25) (2013) 9942.
396 doi:10.1039/c3ra41890a.

397 URL http://xlink.rsc.org/?DOI=c3ra41890a

[8] N. T. Le, P. Lakshmanan, K. Cho, Y. Han, H. Kim, Selective oxidation of 5-hydroxymethyl-2-furfural into 2,5-diformylfuran over VO2+and Cu2+ions immobilized on sulfonated carbon catalysts, Applied Catalysis A: General 464-465 (2013) 305–312. doi:10.1016/j.apcata.2013.06.002.
URL http://dx.doi.org/10.1016/j.apcata.2013.06.002

[9] X. Wan, C. Zhou, J. Chen, W. Deng, Q. Zhang, Y. Yang, Y. Wang, Base-free aerobic oxidation of 5-hydroxymethyl-furfural to 2,5-furandicarboxylic acid in water catalyzed by functionalized carbon nanotube-supported au-pd alloy nanoparticles, ACS Catalysis 4 (7) (2014) 2175–2185. doi:10.1021/cs5003096.

[10] Z. Zhang, J. Zhen, B. Liu, K. Lv, K. Deng, Selective aerobic oxidation of the biomass-derived precursor 5-hydroxymethylfurfural to 2,5-furandicarboxylic acid under mild conditions over a magnetic palladium nanocatalyst, Green Chem. 17 (2) (2015) 1308–1317. doi:10.1039/C4GC01833H.
URL http://xlink.rsc.org/?DOI=C4GC01833H

[11] Avantium, YXY technology for bio-based packaging (2018).
URL https://www.synvina.com/technology/process

[12] N. van Strien, S. Rautiainen, M. Asikainen, D. A. Thomas, J. Linnekoski, K. Niemelä, A. Harlin, A unique pathway to platform chemicals: aldaric acids as stable intermediates for the synthesis of furandicarboxylic acid esters, Green Chemistry 22 (23) (2020) 8271–8277.

[13] V. Choudhary, S. H. Mushrif, C. Ho, A. Anderko, V. Nikolakis, N. S. Marinkovic, A. I. Frenkel, S. I. Sandler, D. G. Vlachos, Insights into the interplay of Lewis and Brønsted acid catalysts in glucose and fructose conversion to 5-(hydroxymethyl) furfural and levulinic acid in aqueous me-

424   dia, Journal of the American Chemical Society 135 (10) (2013) 3997–4006.
425   doi:10.1021/ja3122763.

426 [14] C. Antonetti, M. Melloni, D. Licursi, S. Fulignati, E. Ribechini, S. Rivas,
427   J. C. Parajó, F. Cavani, A. M. Raspolli Galletti, Microwave-assisted dehy-
428   dration of fructose and inulin to HMF catalyzed by niobium and zirconium
429   phosphate catalysts, Applied Catalysis B: Environmental 206 (2017) 364–
430   377. doi:10.1016/j.apcatb.2017.01.056.
431   URL http://dx.doi.org/10.1016/j.apcatb.2017.01.056

432 [15] Y. Li, H. Liu, C. Song, X. Gu, H. Li, W. Zhu, S. Yin, C. Han, The dehydra-
433   tion of fructose to 5-hydroxymethylfurfural efficiently catalyzed by acidic
434   ion-exchange resin in ionic liquid, Bioresource Technology 133 (2013) 347–
435   353. doi:10.1016/j.biortech.2013.01.038.
436   URL http://dx.doi.org/10.1016/j.biortech.2013.01.038

437 [16] H. Zhao, J. E. Holladay, H. Brown, Z. C. Zhang, Metal chlorides in ionic liq-
438   uid solvents convert sugars to 5-hydroxymethylfurfural, Science 316 (5831)
439   (2007) 1597–1600. doi:10.1126/science.1141199.

440 [17] L. Cao, I. K. Yu, S. S. Chen, D. C. Tsang, L. Wang, X. Xiong,
441   S. Zhang, Y. S. Ok, E. E. Kwon, H. Song, C. S. Poon, Production
442   of 5-hydroxymethylfurfural from starch-rich food waste catalyzed by sul-
443   fonated biochar, Bioresource Technology 252 (October 2017) (2018) 76–82.
444   doi:10.1016/j.biortech.2017.12.098.
445   URL https://doi.org/10.1016/j.biortech.2017.12.098

446 [18] M. Bicker, D. Kaiser, L. Ott, H. Vogel, Dehydration of D-fructose to hy-
447   droxymethylfurfural in sub- and supercritical fluids, Journal of Supercriti-
448   cal Fluids 36 (2) (2005) 118–126. doi:10.1016/j.supflu.2005.04.004.

[19] J. K. C. N. Agutaya, R. Inoue, S. S. Vin Tsie, A. T. Quitain, J. de la Pena-Garcia, H. Perez-Sanchez, M. Sasaki, T. Kida, Metal-free synthesis of hmf from glucose using the supercritical co2–subcritical h2o–isopropanol system, Industrial & Engineering Chemistry Research 59 (38) (2020) 16527–16538.

[20] S. K. Patil, C. R. Lund, Formation and growth of humins via aldol addition and condensation during acid-catalyzed conversion of 5-hydroxymethylfurfural, Energy and Fuels 25 (10) (2011) 4745–4755. doi:10.1021/ef2010157.

[21] R. Li, Q. Lin, Y. Wang, W. Yang, X. Liu, W. Li, X. Wang, X. Wang, C. Liu, J. Ren, Brønsted acid-driven conversion of glucose to xylose, arabinose and formic acid via selective c–c cleavage, Applied Catalysis B: Environmental 286 (2021) 119862.

[22] A. Al Ghatta, X. Zhou, G. Casarano, J. D. Wilton-Ely, J. P. Hallett, Characterization and valorization of humins produced by hmf degradation in ionic liquids: A valuable carbonaceous material for antimony removal, ACS Sustainable Chemistry & Engineering (2021).

[23] K. Sun, Y. Shao, Q. Li, L. Zhang, Z. Ye, D. Dong, S. Zhang, Y. Wang, X. Li, X. Hu, Importance of the synergistic effects between cobalt sulfate and tetrahydrofuran for selective production of 5-hydroxymethylfurfural from carbohydrates, Catalysis Science & Technology 10 (7) (2020) 2293–2302.

[24] Y. J. Pagán-Torres, T. Wang, J. M. R. Gallo, B. H. Shanks, J. A. Dumesic, Production of 5-hydroxymethylfurfural from glucose using a combination of lewis and brønsted acid catalysts in water in a biphasic re-

actor with an alkylphenol solvent, ACS Catalysis 2 (6) (2012) 930–934. doi:10.1021/cs300192z.

[25] J. N. Chheda, Y. Román-Leshkov, J. A. Dumesic, Production of 5-hydroxymethylfurfural and furfural by dehydration of biomass-derived mono- and poly-saccharides, Green Chem. 9 (4) (2007) 342–350. doi:10.1039/B611568C.
    URL http://xlink.rsc.org/?DOI=B611568C

[26] E. Taarning, I. Sádaba, P. R. Jensen, S. Meier, Discovery and exploration of the efficient acyclic dehydration of hexoses in dmso/water, ChemSusChem 12 (2019) 5086–5091.

[27] S. Hu, Z. Zhang, Y. Zhou, J. Song, H. Fan, B. Han, Direct conversion of inulin to 5-hydroxymethylfurfural in biorenewable ionic liquids, Green Chemistry 11 (6) (2009) 873. doi:10.1039/b822328a.
    URL http://xlink.rsc.org/?DOI=b822328a

[28] B. Liu, Y. Ren, Z. Zhang, Aerobic oxidation of 5-hydroxymethylfurfural into 2,5-furandicarboxylic acid in water under mild conditions, Green Chem. 17 (3) (2015) 1610–1617. doi:10.1039/C4GC02019G.
    URL http://xlink.rsc.org/?DOI=C4GC02019G

[29] G. Yi, S. P. Teong, Y. Zhang, Base-free conversion of 5-hydroxymethylfurfural to 2,5-furandicarboxylic acid over a Ru/C catalyst, Green Chem. 18 (4) (2016) 979–983. doi:10.1039/C5GC01584G.
    URL http://xlink.rsc.org/?DOI=C5GC01584G

[30] X. Liu, M. Zhang, Z. Li, Coo x-mc (mc= mesoporous carbon) for highly efficient oxidation of 5-hydroxymethylfurfural (5-hmf) to 2, 5-furandicarboxylic acid (fdca), ACS Sustainable Chemistry & Engineering 8 (12) (2020) 4801–4808.

[31] C. Megías-Sayago, A. Lolli, D. Bonincontro, A. Penkova, S. Albonetti, F. Cavani, J. A. Odriozola, S. Ivanova, Effect of gold particles size over au/c catalyst selectivity in hmf oxidation reaction, ChemCatChem 12 (4) (2020) 1177–1183.

[32] F. Koopman, N. Wierckx, J. H. D. Winde, H. J. Ruijssenaars, Bioresource Technology Efficient whole-cell biotransformation of 5-(hydroxymethyl) furfural into FDCA , 2 , 5-furandicarboxylic acid, Bioresource Technology 101 (16) (2010) 6291–6296. doi:10.1016/j.biortech.2010.03.050.
URL http://dx.doi.org/10.1016/j.biortech.2010.03.050

[33] H. Yuan, J. Li, H. dong Shin, G. Du, J. Chen, Z. Shi, L. Liu, Improved production of 2,5-furandicarboxylic acid by overexpression of 5-hydroxymethylfurfural oxidase and 5-hydroxymethylfurfural/furfural oxidoreductase in Raoultella ornithinolytica BF60, Bioresource Technology 247 (August 2017) (2018) 1184–1188. doi:10.1016/j.biortech.2017.08.166.
URL http://dx.doi.org/10.1016/j.biortech.2017.08.166

[34] M. M. Cajnko, U. Novak, M. Grilc, B. Likozar, Enzymatic conversion reactions of 5-hydroxymethylfurfural (hmf) to bio-based 2, 5-diformylfuran (dff) and 2, 5-furandicarboxylic acid (fdca) with air: mechanisms, pathways and synthesis selectivity, Biotechnology for biofuels 13 (2020) 1–11.

[35] Y. Leshkov, J. N. Chheda, J. A. Dumesic, Phase modifiers promote efficient production of hydroxymethylfurfural from fructose, Science 312 (5782) (2006) 1933–1937. doi:10.1126/science.1126337.

[36] G. Shen, B. Andrioletti, Y. Queneau, Furfural and 5-(hydroxymethyl) furfural (hmf): two pivotal intermediates for bio-based chemistry, Current Opinion in Green and Sustainable Chemistry (2020) 100384.

28

[37] A. H. Motagamwala, W. Won, C. Sener, D. M. Alonso, C. T. Maravelias, J. A. Dumesic, Toward biomass-derived renewable plastics: Production of 2,5-furandicarboxylic acid from fructose, Science Advances 4 (1) (2018) eaap9722. doi:10.1126/sciadv.aap9722.

URL http://advances.sciencemag.org/lookup/doi/10.1126/sciadv.aap9722

[38] D. Yan, G. Wang, K. Gao, X. Lu, J. Xin, S. Zhang, One-Pot Synthesis of 2,5-Furandicarboxylic Acid from Fructose in Ionic Liquids, Industrial and Engineering Chemistry Research 57 (6) (2018) 1851–1858. doi:10.1021/acs.iecr.7b04947.

[39] T. Kan, V. Strezov, T. J. Evans, Lignocellulosic biomass pyrolysis: A review of product properties and effects of pyrolysis parameters, Renewable and Sustainable Energy Reviews 57 (2016) 126–1140. doi:10.1016/j.rser.2015.12.185.

URL http://dx.doi.org/10.1016/j.rser.2015.12.185

[40] C. B. Schandel, M. Høj, C. M. Osmundsen, A. D. Jensen, E. Taarning, Thermal cracking of sugars for the production of glycolaldehyde and other small oxygenates, ChemSusChem 13 (4) (2020) 688–692.

[41] C. B. Schandel, M. Høj, C. M. Osmundsen, M. J. Beier, E. Taarning, A. D. Jensen, Kinetic modeling of gas phase sugar cracking to glycolaldehyde and other oxygenates, ACS Sustainable Chemistry & Engineering 9 (1) (2021) 305–311. doi:10.1021/acssuschemeng.0c07232.

[42] D. K. Shen, S. Gu, Pyrolytic behaviour of cellulose in a fluidized bed reactor, Cellulose chemistry and technology 44 (1-3) (2010) 79–87.

[43] K. J. Wu, C. F. Chang, J. S. Chang, Simultaneous production of biohydrogen and bioethanol with fluidized-bed and packed-bed bioreactors con-

taining immobilized anaerobic sludge, Process Biochemistry 42 (7) (2007) 1165–1171. doi:10.1016/j.procbio.2007.05.012.

[44] C. Z. Liu, F. Wang, F. Ou-Yang, Ethanol fermentation in a magnetically fluidized bed reactor with immobilized Saccharomyces cerevisiae in magnetic particles, Bioresource Technology 100 (2) (2009) 878–882. doi:10.1016/j.biortech.2008.07.016.
URL http://dx.doi.org/10.1016/j.biortech.2008.07.016

[45] H. J. S. Lopes, L. R. Ramos, C. A. de Menezes, E. L. Silva, Simultaneous hydrogen and ethanol production in a thermophilic afbr: a comparative approach between cellulosic hydrolysate single fermentation and the fermentation of glucose and xylose as co-substrates, Cellulose 27 (5) (2020) 2599–2612.

[46] T. Ghaznavi, C. Neagoe, G. S. Patience, Partial oxidation of D-xylose to maleic anhydride and acrylic acid over vanadyl pyrophosphate, Biomass and Bioenergy 71 (2014) 285–293. doi:10.1016/j.biombioe.2014.09.029.
URL http://dx.doi.org/10.1016/j.biombioe.2014.09.029

[47] M. Dalil, D. Carnevali, M. Edake, A. Auroux, J. L. Dubois, G. S. Patience, Gas phase dehydration of glycerol to acrolein: Coke on WO_3/TiO_2 reduces by-products, Journal of Molecular Catalysis A: Chemical 421 (2016) 146–155. doi:10.1016/j.molcata.2016.05.022.
URL http://dx.doi.org/10.1016/j.molcata.2016.05.022

[48] D. Carnevali, O. Guévremont, M. G. Rigamonti, M. Stucchi, F. Cavani, G. S. Patience, Gas-Phase Fructose Conversion to Furfural in a Microfluidized Bed Reactor, ACS Sustainable Chemistry & Engineering 6 (4) (2018) 5580–5587. doi:10.1021/acssuschemeng.8b00510.
URL http://pubs.acs.org/doi/10.1021/acssuschemeng.8b00510

[49] M. J. D. Mahboub, J.-L. Dubois, F. Cavani, M. Rostamizadeh, G. S. Patience, Catalysis for the synthesis of methacrylic acid andmethyl methacrylate, Chemical Society Reviews 47 (20) (2018) 7703–7738. doi:10.1039/c8cs00117k.

[50] G. G. Nasr, A. J. Yule, L. Bendig, Industrial sprays and atomization: design, analysis and applications, Springer Science & Business Media, 2013.

[51] C. Orr, J. Dallavalle, Fine Particle Measurement, Macmillan, N.Y., 1959.

[52] D. Geldart, Types of gas fluidization, Powder Technology 7 (5) (1973) 285–292. doi:10.1016/0032-5910(73)80037-3.

[53] A. Tube, S. Chamber, F. C. Assembly, Standard Test Method for Determination of Attrition of FCC Catalysts by Air Jets 1, Tech. rep., ASTM (2013). doi:10.1520/D5757-11.2.

[54] G. S. Patience, R. E. Bockrath, Butane oxidation process development in a circulating fluidized bed, Applied Catalysis A: General 376 (2010) 4–12.

[55] H. Khan, M. G. Rigamonti, G. S. Patience, D. C. Boffito, Spray dried TiO_2/WO_3 heterostructure for photocatalytic applications with residual activity in the dark, Applied Catalysis B: Environmental 226 (2018) 311–323. doi:https://doi.org/10.1016/j.apcatb.2017.12.049.